

PriceFM: Foundation Model for Probabilistic Electricity Price Forecasting

Runyao Yu^{1,2,4}, Chenhui Gu³, Jochen Stiasny², Qingsong Wen⁵,
Wasim Sarwar Dilov⁴, Lianlian Qi^{1,6}, Jochen L. Cremer^{1,2}

¹Austrian Institute of Technology, Vienna, Austria

²Delft University of Technology, Delft, The Netherlands

³Macau University of Science and Technology, Macau, China

⁴Rimac Technology, Zagreb, Croatia

⁵Squirrel Ai Learning, Bellevue, USA

⁶Technical University of Munich, Munich, Germany

Contact Email: runyao.yu@tudelft.nl

Abstract

Electricity price forecasting in Europe presents unique challenges due to the continent's increasingly integrated and physically interconnected power market. While recent advances in deep learning and foundation models have led to substantial improvements in general time series forecasting, most existing approaches fail to capture the complex spatial interdependencies and uncertainty inherent in electricity markets. In this paper, we address these limitations by introducing a comprehensive and up-to-date dataset across 24 European countries (38 regions), spanning from 2022-01-01 to 2025-01-01. Building on this groundwork, we propose PriceFM, a spatiotemporal foundation model that integrates graph-based inductive biases to capture spatial interdependencies across interconnected electricity markets. The model is designed for multi-region, multi-timestep, and multi-quantile probabilistic electricity price forecasting. Extensive experiments and ablation studies confirm the model's effectiveness, consistently outperforming competitive baselines and highlighting the importance of spatial context in electricity markets. The dataset and code can be found at <https://github.com/runyao-yu/PriceFM>.

Introduction

The European electricity market is physically interconnected through a network of cross-border transmission lines, enabling the exchange of electricity between regions and optimizing the social welfare at the European level (Lago et al. 2018). However, physical constraints, such as limited transmission capacity, can restrict electricity flow between regions and lead to zonal price differences (Finck 2021), illustrated in Figure 1. These price disparities highlight the spatial nature of electricity price formation. Recent studies show that electricity price dynamics are strongly influenced by spatial interdependencies and cannot be accurately captured using region-specific models (Do et al. 2024). Therefore, explicitly modeling the spatial structure of the European electricity market is essential for producing accurate price forecasts.

Most existing studies on electricity price forecasting do not explicitly model the spatial structure and focus on a single-region market, particularly Germany (Munian and Ziel 2020; Maciejowska, Nitka, and Weron 2021; Kitsoglou

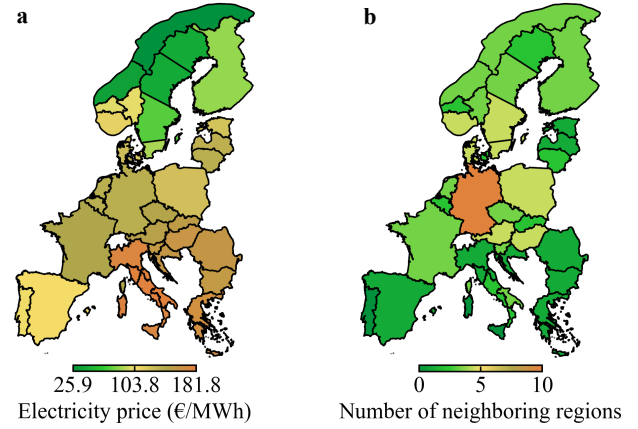


Figure 1: Spatial distribution of electricity price and number of neighboring regions. **a** Electricity prices for 38 European regions averaged from 2022-01-01 to 2025-01-01. A significant zonal price difference is observed between north and south regions. **b** Number of neighboring regions that are directly connected to certain region via transmission lines. For example, France (FR) and Portugal (PT) are directly connected to Spain (ES), thus the number of regions for ES is 2.

et al. 2024), as the German market is one of the largest markets in Europe. Other studies explore forecasting methods for markets such as Denmark, Finland, and Spain, also using region-specific models (Ziel and Weron 2018; Gianfreda, Ravazzolo, and Rossini 2020; Loizidis, Kyprianou, and Georghiou 2024). More recent works explicitly model the spatial nature of the electricity price. For instance, a Graph Convolutional Network (GCN) is applied to capture spatial interdependencies in the Nordic markets, such as Norway, Sweden, and Finland (Yang et al. 2024). Moreover, an attention-based variant is developed to predict prices in certain European markets such as Austria, Germany, and Hungary (Meng et al. 2024). However, these models cover only subsets of Europe and primarily produce point forecasts, failing to capture the uncertainty inherent in electricity prices.

Uncertainty modeling in electricity markets is critical, as

the electricity price is strongly influenced by intermittent renewable generation and fluctuating demand (Lago et al. 2021). Consequently, price forecasting should extend beyond traditional pointwise forecasting to explicitly quantify uncertainties, especially for applications involving risk-sensitive applications such as energy trading and operational planning (Ziel and Steinert 2018). A comprehensive survey summarizes various probabilistic forecasting approaches based on quantile regression methods (Lago et al. 2021). However, these existing methods often focus on single-region markets, thereby neglecting the rich spatial information.

In recent years, foundation models for time series forecasting have achieved remarkable success across diverse domains, demonstrating strong generalization capabilities by capturing complex data patterns (Zhou et al. 2022; Wu et al. 2023; Wang et al. 2024), which makes them attractive candidates for electricity price forecasting. However, existing models are primarily designed for general univariate or multivariate time series tasks and are not explicitly tailored to electricity markets (Liang et al. 2024). Moreover, some foundation models only provide pointwise forecasts and thus fail to capture the uncertainty essential for risk-aware trading decisions in volatile markets. Therefore, addressing the spatial interdependencies and uncertainty in electricity price forecasting within the integrated European market necessitates a tailored foundation model.

To support the development of foundation models for electricity price forecasting, there is a pressing need for high-quality, large-scale, and up-to-date datasets that reflect the spatiotemporal complexity of the integrated European market. However, existing datasets are often fragmented in structure, cover only short time periods, are outdated, or focus on individual regions (Lago et al. 2021). This lack of standardized, cross-border data poses a significant barrier to training and evaluating foundation models.

In this paper, we bridge the gap between recent advances in foundation models and the requirements of electricity price forecasting in spatially interconnected markets. To this end, we introduce a comprehensive and up-to-date dataset capturing key spatiotemporal drivers of electricity prices across Europe. As a step forward, we propose PriceFM, a foundation model that incorporates graph-based inductive biases to learn spatial structures and generate probabilistic forecasts tailored to the integrated European electricity market.

Contribution

- We introduce and release a comprehensive, up-to-date dataset. To the best of our knowledge, this is the largest and most diverse open dataset for European electricity markets, comprising day-ahead electricity prices, load forecasts, and solar and wind power generation forecasts (onshore and offshore), covering 24 European countries (38 regions), spanning from 2022-01-01 to 2025-01-01.
- We propose and release the PriceFM, a novel forecasting framework that integrates prior graph knowledge derived from the spatial topology of the European electricity market. PriceFM supports multi-region, multi-timestep, and multi-quantile probabilistic electricity price forecasting.

- We conduct extensive experiments to evaluate the model’s performance against multiple baselines, and assess the impact of design choices through ablation studies, thereby providing both quantitative evidence of overall performance and empirical insights into optimal configurations.

Preliminary

The forecasting target is $\mathcal{T} = 24$ hourly prices for the delivery day $\mathcal{D} + 1$, using data available before gate closure, typically around midday on day \mathcal{D} . After midday on \mathcal{D} , the electricity prices for $\mathcal{D} + 1$ are published and known. We employ a backward-looking window of size L (e.g. $L = 24$ corresponds to 24 hours from \mathcal{D}), for known electricity prices, denoted as $\mathbf{X}_{r_{in}}^{\text{price}}$. We also include forward-looking exogenous features, such as day-ahead forecasts of load, solar, and wind (onshore and offshore) power generation for $\mathcal{D} + 1$, denoted as $\mathbf{X}_{r_{in}}^{\text{exo}}$, made on \mathcal{D} before gate closure, as well as their historical values over L . The forecasting setup and the choice of feature set are widely used in prior works (Maciejowska 2020; Uniejewski and Weron 2021; Meng et al. 2024), illustrated in Figure 2. Note that this work aims to utilize multi-region inputs to produce multi-region, multi-timestep, and multi-quantile probabilistic electricity price forecasts. Therefore, the input and output are defined as:

- **Input:** $\mathbf{X}_{r_{in}}^{\text{price}} \in \mathbb{R}^{L \times f_1}$ and $\mathbf{X}_{r_{in}}^{\text{exo}} \in \mathbb{R}^{(L+\mathcal{T}) \times f_2}$.
- **Output:** $\hat{\mathbf{y}}_{r_{out}, \tau} \in \mathbb{R}^{\mathcal{T}}$

where $r_{in}, r_{out} \in \mathcal{R} = \{\text{AT}, \dots, \text{SK}\}$ (region codes, detailed in Appendix, Table 1.), $\tau \in \mathcal{Q} = \{0.1, 0.5, 0.9\}$ (quantile levels), $f_1 = 1$, and f_2 varies by region. For example, the forecasted wind power generation is not available in SI.

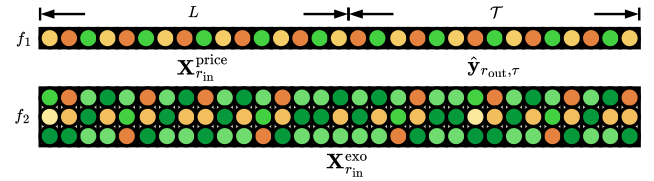


Figure 2: Forecasting setup and feature set.

Data

The dataset is primarily collected from the European Network of Transmission System Operators for Electricity (ENTSO-E). We release the raw and cleaned dataset.

Spatiotemporal Coverage

Spatially, the dataset covers 24 European countries (38 regions). These regions reflect transmission zones rather than administrative boundaries. For example, DK is split into two regions: DK1 and DK2. Each is connected to different neighboring regions, resulting in distinct cross-border power flows. Temporally, the dataset spans from 2022-01-01 to 2025-01-01, providing wide temporal coverage.

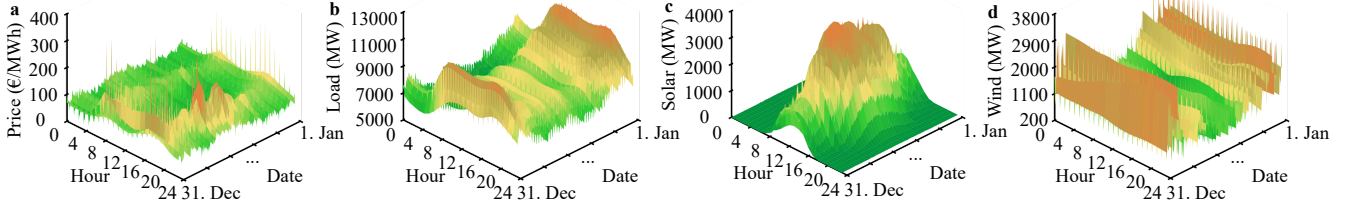


Figure 3: European-level energy data in 2024, averaged across all available regions (depending on data availability). **a** Electricity price. Price spikes sharply during the morning and evening peak, dip around midday, and shows higher volatility in winter. **b** Forecasted load. Load exhibits a clear double-peak each day (in morning and evening) with winter peaks substantially larger than summer. **c** Forecasted solar power generation. Solar is zero overnight, rises in a smooth bell curve to a strong midday maximum, then falls back to zero by dusk, and is much higher in summer. **d** Forecasted wind power generation (sum of onshore and offshore). Wind lacks a daily pattern, fluctuates with high-frequency spikes, and is much higher in the windy winter.

Feature Set

The feature set includes day-ahead electricity prices, load forecasts, and solar and wind power generation forecasts (onshore and offshore). For simplicity, we refer to these features as *price*, *load*, *solar*, and *wind* (*onshore and offshore*), respectively. Importantly, some regions only contain partial features. The full availability of features across regions is detailed in Appendix, Table 1. A European-level visualization of these features is shown in Figure 3.

Resolution

We resample all features in an hourly resolution, as the raw data exhibit a heterogeneous temporal structure. For example, load from ES is provided at an hourly resolution before 2022-05-23 and then switches to a quarter-hourly resolution afterward; the price from AT is reported hourly, while the load is reported quarter-hourly.

Missing Value

Partial features are excluded due to the high rate (above 15%) of missing values, summarized in Appendix, Table 1. For example, wind offshore from FR has a missing rate of 53.2% and is only available after 2023-08-07; solar from LV has a 75.5% missing rate and is only available after 2024-04-07; load from SK has a missing rate of 16.8% and is no longer available after 2024-07-01. For features with low missing rates (around 1%), such as load from EE and SI, we fill them using linear interpolation.

Model

PriceFM, illustrated in Figure 4, aims to produce joint forecasts for multi-region, multi-timestep, and multi-quantile settings. The inputs $\mathbf{X}_{r_{in}}^{\text{price}} \in \mathbb{R}^{L \times f_1}$ and $\mathbf{X}_{r_{in}}^{\text{exo}} \in \mathbb{R}^{(L+\mathcal{T}) \times f_2}$ for input region r_{in} are described in Section *Preliminary*. The inclusion of price and exogenous features introduces heterogeneity along the temporal and feature dimensions.

Backbone

We design a **Fusion Block** to enable effective fusion of heterogeneous multivariate input features and produce a spatial representation, and a **Graph Block** to incorporate prior graph knowledge to enforce spatial decay.

Fusion Block We first align the temporal dimensions by projecting the price feature to length $L + \mathcal{T}$ via a dense layer with linear activation, followed by a transformation into a hidden space of dimension h via k dense layers:

$$\mathbf{X}_{r_{in}}^{\text{price}} \xrightarrow{\text{Project}} \tilde{\mathbf{X}}_{r_{in}}^{\text{price}} \in \mathbb{R}^{(L+\mathcal{T}) \times f_1}, \quad (1)$$

$$\tilde{\mathbf{X}}_{r_{in}}^{\text{price}} \xrightarrow{\text{Dense} \times k} \hat{\mathbf{X}}_{r_{in}}^{\text{price}} \in \mathbb{R}^{(L+\mathcal{T}) \times h}, \quad (2)$$

$$\mathbf{X}_{r_{in}}^{\text{exo}} \xrightarrow{\text{Dense} \times k} \hat{\mathbf{X}}_{r_{in}}^{\text{exo}} \in \mathbb{R}^{(L+\mathcal{T}) \times h}. \quad (3)$$

Next, we perform feature fusion through residual addition and flatten the fused representation to produce the regional representation $\mathbf{F}_{r_{in}}$, which encodes the backward-looking price feature and forward-looking contextual information:

$$\mathbf{F}_{r_{in}} = \text{Flatten}(\hat{\mathbf{X}}_{r_{in}}^{\text{price}} + \hat{\mathbf{X}}_{r_{in}}^{\text{exo}}) \in \mathbb{R}^{(L+\mathcal{T}) \cdot h}. \quad (4)$$

Next, the fused vectors $\mathbf{F}_{r_{in}}$ for all regions $r_{in} \in \mathcal{R}$ are stacked to form a spatial representation:

$$\mathbf{S} = \text{Stack}(\{\mathbf{F}_{r_{in}}\}_{r_{in} \in \mathcal{R}}) \in \mathbb{R}^{|\mathcal{R}| \times (L+\mathcal{T}) \cdot h}. \quad (5)$$

This fusion process enables feature aggregation across input regions with varying temporal and feature dimensions.

Graph Block We first construct *graph distance* by performing a breadth-first search (BFS) traversal on the cross-border grid topology, which records the prior graph knowledge. For a given output region $r_{out} \in \mathcal{R}$, we define the graph distance $d(r_{in}, r_{out})$ as the minimal number of transmission hops from each input region r_{in} to out region r_{out} , based on direct or indirect physical connectivity:

$$d(r_{in}, r_{out}) = \begin{cases} 0 & \text{if } r_{in} = r_{out}, \\ 1 & \text{if } r_{in} \sim r_{out}, \\ 1 + \min_{r' \sim r_{in}} d(r', r_{out}) & \text{otherwise,} \end{cases} \quad (6)$$

where $\mathbf{W}_{r_{\text{out}}} \in \mathbb{R}^{|\mathcal{R}| \times 1}$ is the decay mask vector for r_{out} , and $\mathbf{1} \in \mathbb{R}^{|\mathcal{R}| \times 1}$ is a vector of ones.

This operation acts as spatial regularization and eliminates the need for an exhaustive learning process to determine spatial weights, as required in methods such as attention.

Head

We design a multi-region, multi-timestep, and multi-quantile head, where the model produces joint probabilistic forecasts. To prevent quantile crossing issue¹, we adopt a hierarchical quantile head (Yu et al. 2025). In detail, the median quantile ($\tau = 0.5$) price trajectory, which represents the full set of timesteps \mathcal{T} , is predicted from $\mathbf{U}_{r_{\text{out}}}$ via a dense layer:

$$\hat{\mathbf{y}}_{r_{\text{out}},0.5} = \text{Dense}(\mathbf{U}_{r_{\text{out}}}) \in \mathbb{R}^{\mathcal{T}}. \quad (10)$$

For the upper quantile ($\tau = 0.9$), a residual price trajectory $\hat{\mathbf{r}}_{r_{\text{out}},0.9}$ is predicted from $\mathbf{U}_{r_{\text{out}}}$ via a dense layer:

$$\hat{\mathbf{r}}_{r_{\text{out}},0.9} = \text{Dense}(\mathbf{U}_{r_{\text{out}}}) \in \mathbb{R}^{\mathcal{T}}, \quad (11)$$

where a non-negative function $g(\cdot)$, such as absolute-value function, is applied to the price residual. The upper quantile forecast is obtained by adding this non-negative residual to the median prediction:

$$\hat{\mathbf{y}}_{r_{\text{out}},0.9} = \hat{\mathbf{y}}_{r_{\text{out}},0.5} + g(\hat{\mathbf{r}}_{r_{\text{out}},0.9}). \quad (12)$$

For the lower quantile ($\tau = 0.1$), we compute a residual trajectory similarly:

$$\hat{\mathbf{r}}_{r_{\text{out}},0.1} = \text{Dense}(\mathbf{U}_{r_{\text{out}}}) \in \mathbb{R}^{\mathcal{T}}, \quad (13)$$

and subtract it from the median to obtain the lower quantile prediction:

$$\hat{\mathbf{y}}_{r_{\text{out}},0.1} = \hat{\mathbf{y}}_{r_{\text{out}},0.5} - g(\hat{\mathbf{r}}_{r_{\text{out}},0.1}). \quad (14)$$

This hierarchical design guarantees that the upper quantile prediction is greater than or equal to the lower one at each time step, effectively overcoming quantile crossing.

Loss

We introduce the *Average Quantile Loss (AQL)* as the training objective for multi-region, multi-timestep, and multi-quantile probabilistic forecasting. Let $y_{i,r_{\text{out}},t}$ denote the ground-truth price for the i -th training sample, output region r_{out} , and timestep t , and let $\hat{y}_{i,r_{\text{out}},t,\tau}$ be the corresponding predicted quantile. The AQL across all training samples, regions, timesteps, and quantiles is computed as:

$$\text{AQL} = \frac{1}{N |\mathcal{R}| |\mathcal{T}| |\mathcal{Q}|} \sum_{i=1}^N \sum_{r_{\text{out}} \in \mathcal{R}} \sum_{t=1}^{\mathcal{T}} \sum_{\tau \in \mathcal{Q}} L_{\tau}(y_{i,r_{\text{out}},t}, \hat{y}_{i,r_{\text{out}},t,\tau}), \quad (15)$$

where N is the number of samples, and the quantile loss function L_{τ} for a single prediction task is defined as:

$$L_{\tau}(y, \hat{y}_{\tau}) = \begin{cases} \tau \cdot (y - \hat{y}_{\tau}), & \text{if } y \geq \hat{y}_{\tau}, \\ (1 - \tau) \cdot (\hat{y}_{\tau} - y), & \text{otherwise,} \end{cases} \quad (16)$$

where y and \hat{y} are the true and predicted values, respectively.

A lower AQL indicates more accurate probabilistic forecasting across spatial and temporal dimensions.

¹Quantile crossing refers to the phenomenon where upper quantile predictions (e.g., 90%) fall below lower quantiles (e.g., 10%), violating the monotonicity of the quantile function. (Chernozhukov, Fernández-Val, and Galichon 2010).

Other Details

We use the Adam optimizer with an initial learning rate of 4×10^{-3} , which decays exponentially by a factor of 0.95 every 10 epochs. The batch size is 8, which introduces a slight regularization effect. The model is trained for 50 epochs, and the checkpoint with the lowest validation loss is saved.

Experiment

For the three-year dataset, we use the first two years of the dataset (67%) for training, and the final year (33%) is evenly split into validation and testing sets, strictly preserving the temporal order to ensure realistic out-of-sample evaluation. We assess the model performance using the quantile loss at individual levels (Q10, Q50, and Q90), AQL, Average Quantile Crossing Rate (AQCR), Root Mean Squared Error (RMSE), Mean Absolute Error (MAE), and coefficient of determination (R^2). The Diebold-Mariano (DM) test is applied to determine if two models have a significant difference in the probabilistic and pointwise forecasting (Diebold and Mariano 2002). Each metric is explained in Appendix, Section *Metrics*.

Model Comparison

We include several spatial and temporal models as baselines. Model descriptions and hyperparameter optimization are detailed in Appendix, Section *Baselines*.

Spatial Models Following (Yang et al. 2024; Meng et al. 2024), where variants of GNNs, such as the Graph Convolutional Network (GraphConv) and the Graph Attention Network (GraphAttn), have made successes in electricity price forecasting, we include them as baselines. We also compare with other advanced variants, such as a GNN based on sample-and-aggregate operations (GraphSAGE) (Hamilton, Ying, and Leskovec 2017), a diffusion-based GNN (GraphDiff) (Li et al. 2018), and a GNN with Auto-Regressive Moving Average filters (GraphARMA) (Bianchi et al. 2021).

Results in Table 1 show that PriceFM statistically outperforms all spatial models, confirmed by both the probabilistic and pointwise DM test. A common limitation of these models is that they have only limited spatial priors, relying primarily on data-driven learning to assign spatial importance. Without an explicit mechanism to enforce spatial decay, they lack regularization over noisy regions. As a result, they require large datasets to generalize. However, despite our dataset spanning three years, which is considered large in the domain, the daily forecasting requirement limits the training set to only around 700 samples, making it unsuitable for such models.

Temporal Models We include FEDFormer (Zhou et al. 2022), TimesNet (Wu et al. 2023), and TimeXer (Wang et al. 2024) in our evaluation. As these foundation models do not support graph-based input, features from all regions are concatenated along the feature dimension. Including these models aims to investigate whether these pure time-series models can capture spatial patterns without prior graph knowledge.

Results in Table 1 show that PriceFM statistically outperforms all temporal models, confirmed by the pointwise DM test. In particular, the inclusion of noisy features from weakly

MODEL	Q10 ↓	Q50 ↓	Q90 ↓	AQL ↓	AQCR ↓	RMSE ↓	MAE ↓	R^2 ↑
GRAPHCONV	4.81±0.16	<u>10.76±0.16</u>	7.11±0.33	<u>7.56±0.15</u>	2.19±0.76	<u>35.75±0.60</u>	<u>21.53±0.33</u>	<u>0.51±0.02</u>
GRAPHATTN	5.08±0.31	11.58±0.37	7.90±0.40	8.18±0.29	<u>1.41±0.47</u>	37.63±0.62	23.15±0.75	0.44±0.01
GRAPHSAGE	5.20±0.13	11.27±0.23	7.39±0.35	7.95±0.18	<u>2.79±0.56</u>	37.09±0.81	22.53±0.46	0.47±0.02
GRAPHDIFF	<u>4.80±0.20</u>	11.03±0.21	7.34±0.33	7.73±0.18	3.33±0.70	36.35±0.80	22.07±0.42	0.48±0.02
GRAPHARMA	4.87±0.07	11.10±0.22	<u>7.00±0.22</u>	7.66±0.16	2.05±0.65	36.15±0.59	22.21±0.44	0.49±0.02
FEDFORMER	—	—	—	—	—	47.55±1.51	28.91±0.99	0.14±0.00
TIMESNET	—	—	—	—	—	44.20±0.87	26.40±0.52	0.30±0.01
TIMEKER	—	—	—	—	—	47.38±1.18	28.29±0.71	0.14±0.02
PRICEFM	4.89±0.05	9.83±0.15	5.96±0.08	6.89±0.08	0.00±0.00	32.25±0.38	19.65±0.30	0.61±0.01

Table 1: Model performance comparison on the testing set. The symbol “—” indicates that the model does not support probabilistic forecasting by design. All metrics are reported as mean±standard deviation over 5 independent runs. The best results are shown in **bold**, and the second-best are underlined. The units of Q10, Q50, Q90, AQL, RMSE, and MAE are expressed in €/MWh (denormalized), and AQCR in %.

related regions easily leads to overfitting, given the high model complexity of these time-series foundation models. This observation confirms that the temporal models struggle to recognize spatial patterns without explicit injection of graph knowledge. In contrast, PriceFM incorporates a graph decay mechanism that acts as a spatial regularizer, thereby attenuating the influence of noisy regions.

Ablation Study

We systematically evaluate the impact of key hyperparameters and architectural design choices, including spatiotemporal configurations, fusion strategies in the fusion block, graph decay mechanisms in the graph block, and variants of the hierarchical quantile head.

Spatiotemporal Configurations We assess the impact of two key hyperparameters that control the spatial decay strength and temporal input length:

- **Curvature Parameter:** Spatially, we evaluate $c \in \{-1.0, -0.8, \dots, 0.8, 1.0\}$ in increments of 0.2, ranging from weak decay to strong decay. In total, 2,090 trials are conducted to determine the optimal curvature value for each output region individually, based on validation loss.
- **Backward-Looking Window Size:** Temporally, we compare $L \in \{24, 72, 168\}$, corresponding to one day, three days, and one week. For each window size, all other hyperparameters are re-optimized.

Figure 5 illustrates the testing loss and the distribution of optimal curvature values across all regions. Most regions confirm spatial interdependencies ($c \neq 1.0$). The identified optimal curvature shows a weak negative correlation ($\rho = -0.18$) with the number of directly connected regions, mentioned in Figure 1. The results in Table 2 indicate that the optimal backward-looking window size is 24, potentially because information from the distant past becomes outdated.

Fusion Block We compare the residual addition from the fusion block, described in Eq. (4), with two fusion strategies:

- **Concatenation:** We replace Eq. (4) by first flattening both $\hat{\mathbf{X}}_{r_{in}}^{\text{price}}$ and $\hat{\mathbf{X}}_{r_{in}}^{\text{exo}}$, then concatenating them:

$$\mathbf{F}_{r_{in}} = \text{Concat} \left(\text{Flatten} \left(\hat{\mathbf{X}}_{r_{in}}^{\text{price}} \right), \text{Flatten} \left(\hat{\mathbf{X}}_{r_{in}}^{\text{exo}} \right) \right). \quad (17)$$

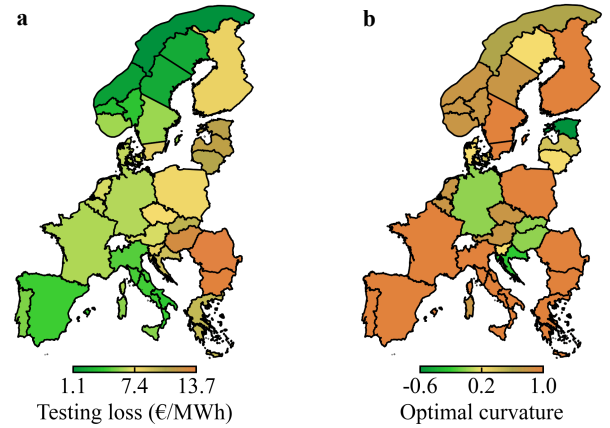


Figure 5: Spatial distribution of testing loss and curvature values. **a** Average quantile loss per region on the testing set. Western European regions exhibit lower losses, whereas BG, HU, and RO show particularly high losses (orange areas). **b** Optimal curvature value per region. Particularly, 8 regions from IT and SE have a curvature value of 1, indicating optimal performance by excluding neighboring features.

- **Cross-Attention:** We apply multi-head attention with $\hat{\mathbf{X}}_{r_{in}}^{\text{price}}$ as the query and $\hat{\mathbf{X}}_{r_{in}}^{\text{exo}}$ as both key and value to produce $\hat{\mathbf{X}}_{r_{in}}^{\text{attn}}$. The attended features are then fused back into the price representation using residual addition:

$$\mathbf{F}_{r_{in}} = \text{Flatten} \left(\hat{\mathbf{X}}_{r_{in}}^{\text{price}} + \hat{\mathbf{X}}_{r_{in}}^{\text{attn}} \right). \quad (18)$$

The results in Table 2 show that replacing the residual addition with concatenation leads to 6.10% higher AQL for probabilistic prediction. Switching to cross-attention yields comparable performance to residual addition, while introducing additional model parameters and unnecessary complexity. This suggests that the residual addition strikes a favorable balance between performance and model simplicity.

Graph Block We compare the graph decay mask from the graph block, described in Eq. (8), with two alternatives:

METHOD	Q10 ↓	Q50 ↓	Q90 ↓	AQL ↓	AQCR ↓	RMSE ↓	MAE ↓	R ² ↑
$L = 24^\dagger$	4.89±0.05	9.83±0.15	5.96±0.08	6.89±0.08	0.00±0.00	32.25±0.38	19.65±0.30	0.61±0.01
$L = 72$	<u>5.09±0.13</u>	<u>10.04±0.20</u>	<u>6.27±0.06</u>	<u>7.14±0.09</u>	0.00±0.00	<u>32.76±0.41</u>	<u>20.09±0.39</u>	<u>0.60±0.01</u>
$L = 168$	<u>5.62±0.30</u>	<u>10.52±0.26</u>	<u>6.65±0.16</u>	<u>7.60±0.21</u>	0.00±0.00	<u>33.82±0.59</u>	<u>21.04±0.53</u>	<u>0.57±0.01</u>
RES. ADD [†]	4.89±0.05	<u>9.83±0.15</u>	5.96±0.08	6.89±0.08	0.00±0.00	32.25±0.38	<u>19.65±0.30</u>	0.61±0.01
CONCAT.	5.03±0.18	10.50±0.21	6.40±0.06	7.31±0.13	0.00±0.00	34.68±0.49	21.01±0.42	0.56±0.01
CROSS-ATTN	<u>4.92±0.14</u>	9.76±0.10	<u>6.07±0.09</u>	<u>6.92±0.09</u>	0.00±0.00	<u>32.46±0.27</u>	19.51±0.19	0.61±0.01
DECAY [†]	4.89±0.05	9.83±0.15	5.96±0.08	6.89±0.08	0.00±0.00	32.25±0.38	19.65±0.30	0.61±0.01
RANDOM	5.32±0.27	<u>10.95±0.13</u>	7.21±0.11	7.83±0.11	0.00±0.00	35.85±0.30	<u>21.89±0.25</u>	<u>0.50±0.02</u>
NO DECAY	<u>5.23±0.32</u>	11.05±0.22	<u>6.84±0.22</u>	<u>7.71±0.16</u>	0.00±0.00	<u>35.81±0.63</u>	22.11±0.44	<u>0.50±0.02</u>
ABS [†]	4.89±0.05	<u>9.83±0.15</u>	<u>5.96±0.08</u>	<u>6.89±0.08</u>	0.00±0.00	32.25±0.38	<u>19.65±0.30</u>	<u>0.61±0.01</u>
SQUARE	4.86±0.14	9.80±0.16	6.05±0.21	6.90±0.15	0.00±0.00	<u>32.35±0.36</u>	19.59±0.33	<u>0.61±0.01</u>
ReLU	4.76±0.15	9.84±0.07	6.06±0.14	6.89±0.07	0.00±0.00	32.48±0.13	19.68±0.15	0.61±0.00
STANDARD	<u>4.80±0.14</u>	10.05±0.06	5.94±0.13	6.93±0.04	<u>4.10±1.28</u>	32.76±0.18	20.10±0.13	0.60±0.01

Table 2: Ablation studies of different module choices: temporal configuration (rows 1-3), fusion block (rows 4-6), graph block (rows 7-9), and hierarchical quantile head (rows 10-13). The symbol [†] marks the method used in PriceFM. All metrics are reported as mean±standard deviation over 5 independent runs. The best results are shown in **bold**, and the second-best are underlined. The units of Q10, Q50, Q90, AQL, RMSE, and MAE are expressed in €/MWh (denormalized), and AQCR in %.

- **Random Graph Decay Mask:** We replace Eq. (8) with a randomly sampled vector, where each decay weight is drawn independently from a uniform distribution over $[0, 1]$, thereby removing the spatial graph prior:

$$\mathbf{W}_{r_{\text{out}}} \sim \mathcal{U}(0, 1)^{|\mathcal{R}| \times 1}. \quad (19)$$

- **No Graph Decay:** We remove the decay mask, which simplifies Eq. (9) to a uniform average over input regions:

$$\mathbf{U}_{r_{\text{out}}} = \frac{\mathbf{1}^\top \mathbf{S}}{|\mathcal{R}|}, \quad (20)$$

The results in Table 2 demonstrate that randomizing or removing the graph decay mask, which discards the prior graph knowledge, leads to a significant drop in all metrics. We also observe that such results, obtained without prior graph knowledge, are on par with those of GNN variants, shown in Table 1. We emphasize that relying on pure data-driven learning without an explicit decay mechanism leads to a loss of the key inductive bias, limiting the model’s performance, especially when the training data is scarce.

Hierarchical Quantile Head We evaluate the impact of different non-negative functions used in Eq. (12) and (14), and include a standard multi-quantile head for comparison.

- **Non-Negative Functions:** We replace the absolute-value function with either a square function or ReLU:

$$g(\cdot) = (\cdot)^2, \quad (21)$$

$$g(\cdot) = \max(0, \cdot). \quad (22)$$

- **Standard Multi-Quantile Head:** The Eq. (11) and (13) are skipped, and the shared representation $\mathbf{U}_{r_{\text{out}}}$ is passed directly to three independent dense layers to produce each quantile trajectory:

$$\hat{\mathbf{y}}_{r_{\text{out}}, 0.1} = \text{Dense}(\mathbf{U}_{r_{\text{out}}}) \in \mathbb{R}^{\mathcal{T}}, \quad (23)$$

$$\hat{\mathbf{y}}_{r_{\text{out}}, 0.5} = \text{Dense}(\mathbf{U}_{r_{\text{out}}}) \in \mathbb{R}^{\mathcal{T}}, \quad (24)$$

$$\hat{\mathbf{y}}_{r_{\text{out}}, 0.9} = \text{Dense}(\mathbf{U}_{r_{\text{out}}}) \in \mathbb{R}^{\mathcal{T}}. \quad (25)$$

The results in Table 2 reveal that replacing the absolute-value function with either a square function or ReLU does not result in a noticeable change in performance, suggesting that the choice of non-negative function is flexible. Moreover, while the hierarchical quantile head achieves comparable loss to the standard multi-quantile head, the latter exhibits a mean AQCR of 4.10%, indicating that the hierarchical design mitigates quantile crossing without harming performance.

Conclusion

In this paper, we introduced and released a dataset, which will benefit both the research community and the energy industry. We proposed and released PriceFM, a foundation model tailored for interconnected European electricity markets. Extensive experiments and ablation studies demonstrate that PriceFM outperforms competitive baselines and highlight the importance of spatial context. By enabling more accurate and comprehensive probabilistic electricity price forecasting, our work has the potential to support better decision-making in energy trading and grid management, contributing to a more efficient and resilient energy ecosystem.

Despite these promising results, our study has two key limitations. First, the graph decay function is empirically designed; the performance may improve with alternative functions. Second, PriceFM relies on the current transmission topology, which may become outdated as transmission networks evolve, requiring retraining to adapt to new scenarios.

References

- Bianchi, F. M.; Grattarola, D.; Livi, L.; and Alippi, C. 2021. Graph neural networks with convolutional arma filters. *IEEE transactions on pattern analysis and machine intelligence*, 44(7): 3496–3507.
- Chernozhukov, V.; Fernández-Val, I.; and Galichon, A. 2010.

- Quantile and Probability Curves Without Crossing. *Econometrica*, 78(3): 1093–1125.
- Diebold, F. X.; and Mariano, R. S. 2002. Comparing predictive accuracy. *Journal of Business & economic statistics*, 20(1): 134–144.
- Do, H. X.; Nepal, R.; Pham, S. D.; and Jamasb, T. 2024. Electricity market crisis in Europe and cross border price effects: A quantile return connectedness analysis. *Energy Economics*, 135: 107633.
- Finck, R. 2021. Impact of flow based market coupling on the European electricity markets. In *Sustainability Management Forum—NachhaltigkeitsManagementForum*, volume 29, 173–186. Springer.
- Gianfreda, A.; Ravazzolo, F.; and Rossini, L. 2020. Comparing the Forecasting Performances of Linear Models for Electricity Prices with High RES Penetration. *International Journal of Forecasting*, 36(3): 974–986.
- Hamilton, W.; Ying, Z.; and Leskovec, J. 2017. Inductive Representation Learning on Large Graphs. In Guyon, I.; Luxburg, U. V.; Bengio, S.; Wallach, H.; Fergus, R.; Vishwanathan, S.; and Garnett, R., eds., *Advances in Neural Information Processing Systems*, volume 30. Curran Associates, Inc.
- Kitsatoglou, A.; Georgopoulos, G.; Papadopoulos, P.; and Antonopoulos, H. 2024. An Ensemble Approach for Enhanced Day-Ahead Price Forecasting in Electricity Markets. *Expert Systems with Applications*, 256: 124971.
- Lago, J.; De Ridder, F.; Vrancx, P.; and De Schutter, B. 2018. Forecasting day-ahead electricity prices in Europe: The importance of considering market integration. *Applied energy*, 211: 890–903.
- Lago, J.; Marcjasz, G.; De Schutter, B.; and Weron, R. 2021. Forecasting day-ahead electricity prices: A review of state-of-the-art algorithms, best practices and an open-access benchmark. *Applied Energy*, 293: 116983.
- Li, Y.; Yu, R.; Shahabi, C.; and Liu, Y. 2018. Diffusion Convolutional Recurrent Neural Network: Data-Driven Traffic Forecasting. In *International Conference on Learning Representations*.
- Liang, Y.; Wen, H.; Nie, Y.; Jiang, Y.; Jin, M.; Song, D.; Pan, S.; and Wen, Q. 2024. Foundation models for time series analysis: A tutorial and survey. In *Proceedings of the 30th ACM SIGKDD conference on knowledge discovery and data mining*, 6555–6565.
- Loizidis, S.; Kyprianou, A.; and Georghiou, G. E. 2024. Electricity Market Price Forecasting Using ELM and Bootstrap Analysis: A Case Study of the German and Finnish Day-Ahead Markets. *Applied Energy*, 363: 123058.
- Maciejowska, K. 2020. Assessing the impact of renewable energy sources on the electricity price level and variability – A quantile regression approach. *Energy Economics*, 85: 104532.
- Maciejowska, K.; Nitka, W.; and Weron, T. 2021. Enhancing Load, Wind and Solar Generation for Day-Ahead Forecasting of Electricity Prices. *Energy Economics*, 99: 105273.
- Meng, A.; Zhu, J.; Yan, B.; and Yin, H. 2024. Day-ahead electricity price prediction in multi-price zones based on multi-view fusion spatio-temporal graph neural network. *Applied Energy*, 369: 123553.
- Munian, P.; and Ziel, F. 2020. Probabilistic forecasting in day-ahead electricity markets: Simulating peak and off-peak prices. *International Journal of Forecasting*, 36(4): 1193–1210.
- Uniejewski, B.; and Weron, R. 2021. Regularized Quantile Regression Averaging for Probabilistic Electricity Price Forecasting. *Energy Economics*, 95: 105121.
- Wang, Y.; Wu, H.; Dong, J.; Qin, G.; Zhang, H.; Liu, Y.; Qiu, Y.; Wang, J.; and Long, M. 2024. TimeXer: Empowering Transformers for Time Series Forecasting with Exogenous Variables. In Globerson, A.; Mackey, L.; Belgrave, D.; Fan, A.; Paquet, U.; Tomczak, J.; and Zhang, C., eds., *Advances in Neural Information Processing Systems*, volume 37, 469–498. Curran Associates, Inc.
- Wu, H.; Hu, T.; Liu, Y.; Zhou, H.; Wang, J.; and Long, M. 2023. TimesNet: Temporal 2D-Variation Modeling for General Time Series Analysis. In *The Eleventh International Conference on Learning Representations*.
- Yang, Y.; Guo, J.; Li, Y.; and Zhou, J. 2024. Forecasting day-ahead electricity prices with spatial dependence. *International Journal of Forecasting*, 40(3): 1255–1270.
- Yu, R.; Tao, Y.; Leimgruber, F.; Esterl, T.; and Cremer, J. L. 2025. OrderFusion: Encoding Orderbook for End-to-End Probabilistic Intraday Electricity Price Prediction. *arXiv preprint arXiv:2502.06830*.
- Zhou, T.; Ma, Z.; Wen, Q.; Wang, X.; Sun, L.; and Jin, R. 2022. FEDformer: Frequency Enhanced Decomposed Transformer for Long-term Series Forecasting. In Chaudhuri, K.; Jegelka, S.; Song, L.; Szepesvari, C.; Niu, G.; and Sabato, S., eds., *Proceedings of the 39th International Conference on Machine Learning*, volume 162 of *Proceedings of Machine Learning Research*, 27268–27286. PMLR.
- Ziel, F.; and Steinert, R. 2018. Probabilistic mid- and long-term electricity price forecasting. *Renewable and Sustainable Energy Reviews*, 94: 251–266.
- Ziel, F.; and Weron, R. 2018. Day-ahead electricity price forecasting with high-dimensional structures: Univariate vs. multivariate modeling frameworks. *Energy Economics*, 70: 396–420.

Appendix

Code Guideline

We open-source all code for preprocessing, modeling, and analysis. The project directory is structured as follows:

```
| - PriceFM/  
  | - Data/  
  | - Model/  
  | - Result/  
  | - PriceFM.py  
  | - Main.py  
  | - README.md
```

where the README.md specifies the required package version. To facilitate reproducibility and accessibility, we have streamlined the entire pipeline through extensive engineering efforts into just three simple steps:

Step 1: Create a folder named PriceFM, along with subfolders Data, Model, and Result. Place the energy data EU_Spatiotemporal_Energy_Data.csv into Data, and place PriceFM.py inside the PriceFM folder.

Step 2: Run Main.py to process the energy data, and to train, validate, and test the PriceFM. The script PriceFM.py contains all necessary functions and classes.

Step 3: After execution, check the Model and Result folders for the saved model weights and evaluation metrics.

Hardware and Computation

The PriceFM is evaluated on both an NVIDIA A100 GPU and an Intel Core i7-1265U CPU, respectively. The NVIDIA A100 is designed for high-performance computing and deep learning workloads, offering 80 GB of high-bandwidth memory and up to 6,912 CUDA cores. In contrast, the Intel i7-1265U is a power-efficient CPU commonly found in standard laptops. This dual evaluation setup allows us to assess the feasibility of deploying our model in environments without access to advanced GPU hardware.

Under the training setup described in Section *Model*, the training time is approximately 4–5 minutes on the A100 GPU and 12–13 minutes on the i7 CPU. Due to the small batch size used, the GPU does not achieve a significant speedup over the CPU. Inference time for both setups is under 10 seconds. We note that neither training nor inference time is critical for our application, as bid submissions can occur at any point before the market gate closure.

Lookup Table and Feature Availability

The country-region code lookup table and the feature availability are listed in Table 1.

Baselines

We compare the PriceFM with several spatial and temporal models. The PriceFM is optimized based on validation loss, and the hyperparameter search space is summarized in Table 2. The number of parameters of PriceFM is only 3.38M.

The spatial models, such as GraphConv, GraphAttn, GraphDiff, GraphSAGE, and GraphARMA, lack an explicit spatial decay mechanism guided by graph distance. GraphConv assigns uniform weights to all neighbors, ignoring spatial relevance; GraphAttn learns attention weights entirely

from data without structural priors; GraphDiff uses diffusion kernels that spread information globally, but the importance of nodes is still determined through learned weights, without decay constraints; GraphSAGE aggregates features from sampled neighbors but lacks a notion of spatial proximity; and GraphARMA applies recursive smoothing, which can propagate noise from irrelevant neighbors. As a result, these models require large datasets to recognize spatial patterns and may struggle to suppress the influence of noisy regions. The hyperparameters are optimized based on validation loss, and the search space is summarized in Table 3. All spatial models require an adjacency matrix as input, detailed in Section *Spatial Topology and Adjacency Matrix*. Notably, these optimized spatial models contain more than 10M parameters.

FEDFormer, TimesNet, and TimeXer have demonstrated strong performance in general time-series forecasting tasks. FEDFormer and TimeXer are Transformer-based architectures, while TimesNet is CNN-based. However, these models are not designed for spatial graph forecasting tasks and may require large-scale data to implicitly learn spatial dependencies. The hyperparameters are optimized based on validation loss, and the search space is summarized in Table 4. Notably, the number of parameters of these optimized temporal models ranges from 5M to 10M, and they are limited to single-region prediction. As a result, 38 separate models must be trained for each output region, since they are not designed to support multi-region forecasting.

Spatial Topology and Adjacency Matrix

We model the European market as a graph $G = (\mathcal{R}, \mathcal{E})$, where each node $r \in \mathcal{R}$ is a bidding zone and edges indicate direct power flow via cross-border interconnections. This spatial topology is detailed in Table 5.

Let $\mathcal{N}(r)$ denote the set of directly connected neighbors of r , excluding r itself. The binary adjacency matrix $A \in \{0, 1\}^{|\mathcal{R}| \times |\mathcal{R}|}$ is defined by

$$A_{r,s} = \begin{cases} 1, & \text{if } s \in \mathcal{N}(r), \\ 0, & \text{otherwise,} \end{cases} \quad r, s \in \mathcal{R}. \quad (26)$$

For GNN layers, self-loops can be added via $\tilde{A} = A + I$.

Scaling

To normalize the data while being robust to extreme values, we employ a RobustScaler fitted on the training data, using the Scikit-Learn implementation. The fitted scaler is then used to transform validation and testing data.

Metrics

We evaluate the model using Q10, Q50, Q90, AQL, AQCR, RMSE, MAE, and R^2 , all averaged over regions and samples.

Q10, Q50, Q90 We compute quantile loss separately for each target quantile. For example, the Q10 loss is:

$$Q10 = \frac{1}{N|\mathcal{R}|\mathcal{T}} \sum_{i=1}^N \sum_{r_{\text{out}} \in \mathcal{R}} \sum_{t=1}^{\mathcal{T}} L_{0.1}(y_{i,r_{\text{out}},t}, \hat{y}_{i,r_{\text{out}},t,0.1}), \quad (27)$$

and similarly for Q50 and Q90 with $\tau = 0.5$ and 0.9.

COUNTRY	REGION CODE	PRICE	LOAD	SOLAR	WIND (ONSHORE)	WIND (OFFSHORE)
AUSTRIA	AT	✓	✓	✓	✓	
BELGIUM	BE	✓	✓	✓	✓	✓
BULGARIA	BG	✓	✓	✓	✓	
CZECH REPUBLIC	CZ	✓	✓	✓		
GERMANY, LUXEMBOURG	DE-LU	✓	✓	✓	✓	✓
DENMARK	DK1	✓	✓	✓	✓	✓
DENMARK	DK2	✓	✓	✓	✓	✓
ESTONIA	EE	✓	✓	✓	✓	
SPAIN	ES	✓	✓	✓	✓	
FINLAND	FI	✓	✓	✓	✓	
FRANCE	FR	✓	✓	✓	✓	(✓)
GREECE	GR	✓	✓	✓	✓	
CROATIA	HR	✓	✓	✓	✓	
HUNGARY	HU	✓	✓	✓	✓	
ITALY	IT-CALA	✓	✓	✓	✓	
ITALY	IT-CNOR	✓	✓	✓	✓	
ITALY	IT-CSUD	✓	✓	✓	✓	
ITALY	IT-NORD	✓	✓	✓	✓	
ITALY	IT-SARD	✓	✓	✓	✓	
ITALY	IT-SICI	✓	✓	✓	✓	
ITALY	IT-SUD	✓	✓	✓	✓	
LITHUANIA	LT	✓	✓	✓	✓	
LATVIA	LV	✓	✓	(✓)	✓	
NETHERLANDS	NL	✓	✓	✓	✓	✓
NORWAY	NO1	✓	✓		✓	
NORWAY	NO2	✓	✓		✓	
NORWAY	NO3	✓	✓		✓	
NORWAY	NO4	✓	✓		✓	
NORWAY	NO5	✓	✓			
POLAND	PL	✓	✓	✓	✓	
PORTUGAL	PT	✓	✓	✓	✓	✓
ROMANIA	RO	✓	✓	✓	✓	
SWEDEN	SE1	✓	✓	✓	✓	
SWEDEN	SE2	✓	✓	✓	✓	
SWEDEN	SE3	✓	✓	✓	✓	
SWEDEN	SE4	✓	✓	✓	✓	
SLOVENIA	SI	✓	✓	✓		
SLOVAKIA	SK	✓	(✓)	✓	✓	

Table 1: Lookup table and feature availability across European regions. ✓ indicates that the feature is available. (✓) denotes partial availability, and the feature is excluded from this study due to the high rate of missing values.

Table 2: Hyperparameter search space for PriceFM.

Model	Search Space
PriceFM	hidden_size: {12, 24, 48} layers: {2, 3, 4} batch_size: {8, 32, 128} learning_rate: {4e-4, 1e-3, 4e-3} epochs: 50

AQL AQL represents the average quantile loss across all quantiles, as described in Section *Model*.

AQCR AQCR captures the proportion of forecasted distributions that violate quantile monotonicity, i.e., when a higher quantile is predicted to be smaller than a lower one.

The quantile crossing indicator for a quantile pair (τ_l, τ_u) with $\tau_l < \tau_u$ is defined as:

$$C_{\tau_l, \tau_u}(i, r, t) = \mathbb{1}[\hat{y}_{i,r,t,\tau_l} > \hat{y}_{i,r,t,\tau_u}], \quad (28)$$

where $\mathbb{1}[\cdot]$ is the indicator function. Then, the AQCR is given by:

$$\text{AQCR} = \frac{1}{N |\mathcal{R}| \mathcal{T}} \sum_{i=1}^N \sum_{r \in \mathcal{R}} \sum_{t=1}^{\mathcal{T}} \text{Cross}_{i,r,t}. \quad (29)$$

RMSE We compute RMSE within each region, then average over all regions:

$$\text{RMSE}_r = \sqrt{\frac{1}{N \mathcal{T}} \sum_{i=1}^N \sum_{t=1}^{\mathcal{T}} (y_{i,r,t} - \hat{y}_{i,r,t,0.5})^2}, \quad (30)$$

$$\text{RMSE} = \frac{1}{|\mathcal{R}|} \sum_{r \in \mathcal{R}} \text{RMSE}_r. \quad (31)$$

Table 3: Hyperparameter search space for spatial models.

Model	Search Space
GraphConv	hidden_size: {32, 128, 512} layers: {2, 3, 4} batch_size: {8, 32, 128} learning_rate: {4e-4, 1e-3, 4e-3} epochs: 50
GraphAttn	hidden_size: {32, 128, 512} layers: {2, 3, 4} n_heads: {2, 4, 8} batch_size: {8, 32, 128} dropout: {0.1, 0.3, 0.5} learning_rate: {4e-4, 1e-3, 4e-3} epochs: 50
GraphSAGE	hidden_size: {32, 128, 512} layers: {2, 3, 4} aggregate: {mean, max, sum} batch_size: {8, 32, 128} learning_rate: {4e-4, 1e-3, 4e-3} epochs: 50
GraphDiff	diff_steps: {2, 4, 6} hidden_size: {32, 128, 512} layers: {2, 3, 4} batch_size: {8, 32, 128} learning_rate: {4e-4, 1e-3, 4e-3} epochs: 50
GraphARMA	hidden_size: {32, 128, 512} layers: {2, 3, 4} order: {1, 2, 4} iteration: {1, 2, 4} batch_size: {8, 32, 128} learning_rate: {4e-4, 1e-3, 4e-3} epochs: 50

MAE Same procedure as RMSE, but using absolute error:

$$\text{MAE}_r = \frac{1}{N\mathcal{T}} \sum_{i=1}^N \sum_{t=1}^{\mathcal{T}} |y_{i,r,t} - \hat{y}_{i,r,t,0.5}|, \quad (32)$$

$$\text{MAE} = \frac{1}{|\mathcal{R}|} \sum_{r \in \mathcal{R}} \text{MAE}_r. \quad (33)$$

R^2 We compute R^2 for each region and average across all regions:

$$R_r^2 = 1 - \frac{\sum_{i=1}^N \sum_{t=1}^{\mathcal{T}} (y_{i,r,t} - \hat{y}_{i,r,t,0.5})^2}{\sum_{i=1}^N \sum_{t=1}^{\mathcal{T}} (y_{i,r,t} - \bar{y}_r)^2}, \quad (34)$$

$$\bar{y}_r = \frac{1}{N\mathcal{T}} \sum_{i=1}^N \sum_{t=1}^{\mathcal{T}} y_{i,r,t}, \quad (35)$$

$$R^2 = \frac{1}{|\mathcal{R}|} \sum_{r \in \mathcal{R}} R_r^2. \quad (36)$$

Table 4: Hyperparameter search space for temporal models.

Model	Search Space
FEDFormer	hidden_size: {32, 128, 512} conv_hidden_size: {32, 128, 512} e_layers: {2, 3, 4} n_heads: {2, 4, 8} dropout: {0.1, 0.3, 0.5} batch_size: {8, 32, 128} learning_rate: {4e-4, 1e-3, 4e-3} epochs: 50
TimesNet	hidden_size: {32, 128, 512} conv_hidden_size: {32, 128, 512} e_layers: {2, 3, 4} dropout: {0.1, 0.3, 0.5} batch_size: {8, 32, 128} learning_rate: {4e-4, 1e-3, 4e-3} Epochs: 50
TimeXer	hidden_size: {32, 128, 512} e_layers: {2, 3, 4} n_heads: {2, 4, 8} d_ff: {512, 1024, 2048} dropout: {0.1, 0.3, 0.5} batch_size: {8, 32, 128} learning_rate: {4e-4, 1e-3, 4e-3} epochs: 50

DM Test

To assess whether differences in forecasting performance are statistically significant, we apply the DM test. We compute the loss differential at each prediction instance.

For probabilistic forecasts, we compute the loss differential at each quantile $\tau \in \mathcal{Q}$ between two models $l \in \{1, 2\}$:

$$d_{i,r,t,\tau} = L_\tau(y_{i,r,t}, \hat{y}_{i,r,t,\tau}^{(1)}) - L_\tau(y_{i,r,t}, \hat{y}_{i,r,t,\tau}^{(2)}). \quad (37)$$

For point forecasts, the loss differential between two models is computed for each sample, region, and timestep as:

$$d_{i,r,t} = |y_{i,r,t} - \hat{y}_{i,r,t}^{(1)}| - |y_{i,r,t} - \hat{y}_{i,r,t}^{(2)}|. \quad (38)$$

The DM test statistic is then calculated as:

$$\text{DM} = \frac{\bar{d}}{\hat{\sigma}_d / \sqrt{M}}, \quad (39)$$

$$\bar{d} = \frac{1}{M} \sum_{j=1}^M d_j, \quad (40)$$

where $M = N \cdot |\mathcal{R}| \cdot \mathcal{T} \cdot |\mathcal{Q}|$ for probabilistic forecasts, and $M = N \cdot |\mathcal{R}| \cdot \mathcal{T}$ for point forecasts. The index j enumerates all prediction instances across dimensions, and $\hat{\sigma}_d$ is the sample standard deviation of $\{d_j\}_{j=1}^M$.

We compute a two-sided p -value using the Student's t -distribution with $M - 1$ degrees of freedom. A significantly positive (negative) DM value indicates that model 2 (model 1) significantly outperforms the other.

Table 5: Direct neighbors by region and neighbor count.

REGION CODE	DIRECT NEIGHBORS	COUNT
AT	CZ, DE-LU, HU, IT-NORD, SI	5
BE	DE-LU, FR, NL	3
BG	GR, RO	2
CZ	AT, DE-LU, PL, SK	4
DE-LU	AT, BE, CZ, DK1, DK2, FR, NL, NO2, PL, SE4	10
DK1	DE-LU, DK2, NL, NO2, SE3	5
DK2	DE-LU, DK1, SE4	3
EE	FI, LV	2
ES	FR, PT	2
FI	EE, NO4, SE1, SE3	4
FR	BE, DE-LU, ES, IT-NORD	4
GR	BG, IT-SUD	2
HR	HU, SI	2
HU	AT, HR, RO, SI, SK	5
IT-CALA	IT-SICI, IT-SUD	2
IT-CNOR	IT-CSUD, IT-NORD	2
IT-CSUD	IT-CNOR, IT-SARD, IT-SUD	3
IT-NORD	AT, FR, IT-CNOR, SI	4
IT-SARD	IT-CSUD	1
IT-SICI	IT-CALA	1
IT-SUD	GR, IT-CALA, IT-CSUD	3
LT	LV, PL, SE4	3
LV	EE, LT	2
NL	BE, DK1, DE-LU, NO2	4
NO1	NO2, NO3, NO5, SE3	4
NO2	DE-LU, DK1, NL, NO1, NO5	5
NO3	NO1, NO4, NO5, SE2	4
NO4	FI, NO3, SE1, SE2	4
NO5	NO1, NO2, NO3	3
PL	CZ, DE-LU, LT, SE4, SK	5
PT	ES	1
RO	BG, HU	2
SE1	FI, NO4, SE2	3
SE2	NO3, NO4, SE1, SE3	4
SE3	DK1, FI, NO1, SE2, SE4	5
SE4	DE-LU, DK2, LT, PL, SE3	5
SI	AT, HR, HU, IT-NORD	4
SK	CZ, HU, PL	3